Nanoscale Advances

ROYAL SOCIETY OF CHEMISTRY

PAPER

View Article Online
View Journal | View Issue

Check for updates

Cite this: *Nanoscale Adv.*, 2021, **3**, 1767

Chemical and topographical patterns combined with solution shear for selective-area deposition of highly-aligned semiconducting carbon nanotubes†

Jonathan H. Dwyer,[a] Anjali Suresh,[b] Katherine R. Jinkins,[b] Xiaoqi Zheng,[b] Michael S. Arnold,*[b] Arganthaël Berson*[c] and Padma Gopalan*[ab]

Selective deposition of semiconducting carbon nanotubes (s-CNTs) into densely packed, aligned arrays of individualized s-CNTs is necessary to realize their potential in semiconductor electronics. We report the combination of chemical contrast patterns, topography, and pre-alignment of s-CNTs *via* shear to achieve selective-area deposition of aligned arrays of s-CNTs. Alternate stripes of surfaces favorable and unfavorable to s-CNT adsorption were patterned with widths varying from 2000 nm down to 100 nm. Addition of topography to the chemical contrast patterns combined with shear enabled the selective-area deposition of arrays of quasi-aligned s-CNTs (~14°) even in patterns that are wider than the length of individual nanotubes (>500 nm). When the width of the chemical and topographical contrast patterns is less than the length of individual nanotubes (<500 nm), confinement effects become dominant enabling the selective-area deposition of much more tightly aligned s-CNTs (~7°). At a trench width of 100 nm, we demonstrate the lowest standard deviation in alignment degree of 7.6 ± 0.3° at a deposition shear rate of 4600 s^{-1}, while maintaining an individualized s-CNT density greater than 30 CNTs μm^{-1}. Chemical contrast alone enables selective-area deposition, but chemical contrast in addition to topography enables more effective selective-area deposition and stronger confinement effects, with the advantage of removal of nanotubes deposited in spurious areas *via* selective lift-off of the topographical features. These findings provide a methodology that is inherently scalable, and a means to deposit spatially selective, aligned s-CNT arrays for next-generation semiconducting devices.

Received 12th January 2021
Accepted 5th February 2021

DOI: 10.1039/d1na00033k

rsc.li/nanoscale-advances

Open Access Article. Published on 17 February 2021. Downloaded on 5/5/2026 7:21:35 PM.
This article is licensed under a Creative Commons Attribution-NonCommercial 3.0 Unported Licence.

1. Introduction

Semiconducting single-walled carbon nanotubes (s-CNTs) are excellent candidates for next-generation field-effect transistors (FETs) due to their outstanding properties such as ballistic transport, excellent charge mobility, and high thermal conductivity.[1–7] However, to date, the vast majority of s-CNT-based FETs have underperformed compared with conventional Si- and GaAs-based FETs due to two main factors. One of these factors is the need to achieve greater than 99.99% semiconducting CNTs from an electronically heterogenous CNT mixture. This material processing challenge has been largely overcome through a number of sorting agents in both aqueous and organic solvents.[8,9] The second issue, which has yet to be reliably solved, relates to the difficulty of scaling single s-CNT devices to s-CNT array devices. An ideal s-CNT array requires deposition to be spatially controlled with a pitch of 5–10 nm (corresponding to 100–200 CNTs μm^{-1} density), while tightly aligning s-CNTs, preventing their overlap and achieving parallel alignment to each other.[5–7,10]

Two primary pathways are typically utilized in the literature to obtain aligned s-CNT arrays: (1) direct growth of s-CNT array through chemical vapor deposition (CVD), and (2) s-CNT deposition from solution. CVD growth uses CNT growth precursors on catalytic substrates to fabricate aligned s-CNT arrays.[11–15] Advantages to CVD method include high degrees of s-CNT alignment in arrays as well as the relative ease of patterning catalytic materials for localized s-CNT growth. Densities as high as 130 CNTs μm^{-1} have been achieved,[14] which is in the predicted optimal density range for s-CNT-based electronics. However, the major disadvantage of the CVD growth method is the concurrent growth of both s-CNTs and metallic CNTs (m-CNTs), hence lowering current on/off ratios.[16] Although progress has been made in selectively synthesizing s-CNTs using CVD[17,18] and removing m-CNTs post-synthetically,[15] the purity levels do not approach those required for high-performing s-CNT-based devices.[7] In addition, most CVD s-

[a]*Department of Chemical and Biological Engineering, University of Wisconsin–Madison, 1415 Engineering Drive, Madison, WI 53706, USA*

[b]*Department of Materials Science and Engineering, University of Wisconsin–Madison, 1509 University Avenue, Madison, WI 53706, USA. E-mail: pgopalan@wisc.edu*

[c]*Multiphase Flow Visualization and Analysis Laboratory (MFVAL), University of Wisconsin–Madison, 1500 Engineering Drive, Madison, WI 53706, USA. E-mail: arganthael.berson@wisc.edu*

† Electronic supplementary information (ESI) available. See DOI: 10.1039/d1na00033k

© 2021 The Author(s). Published by the Royal Society of Chemistry

Open Access Article. Published on 17 February 2021. Downloaded on 5/5/2026 7:21:35 PM.
This article is licensed under a Creative Commons Attribution-NonCommercial 3.0 Unported Licence.

CNT growth mechanisms require specific substrates such as sapphire[11,14] and quartz.[12] Thus, an additional CNT array transfer step is needed to deposit CVD grown s-CNTs on traditional MOSFET substrates like Si wafers.

In contrast to CVD growth mechanisms, s-CNT purities greater than 99.99% are attainable by dispersing s-CNTs in solution to create "inks".[8] To overcome inter-CNT π–π interactions to individualize and deaggregate s-CNTs, typically dispersing agents are necessary. Dispersants such as aromatic conjugated polymers which interact non-covalently with CNTs are also able to sort CNT soot into high-purity, electronics-grade s-CNT inks.[9,19] From these inks, alignment of s-CNTs on substrates has been achieved through various methods including Langmuir–Blodgett/Schaefer,[20–22] vacuum filtration,[23] electric fields,[24–26] shear,[24,27,28] evaporation,[29–32] 3D printing,[33,34] and at liquid/liquid interfaces.[35–37] While these studies have made progress in fabricating continuously aligned s-CNTs on wafer-scale areas, selective-area deposition and controlling their pitch in a scalable manner are still unresolved.

Current selective-area CNT deposition methods include covalent bonding with the substrate,[38,39] tailored electrostatic interactions between the polymer wrapper and the substrate,[28] and use of DNA-based nanotrench guides.[40] Park *et al.* used a blade shearing method to deposit polythiophene-wrapped s-CNT arrays selectively on a substrate with alternating patterns of 500 nm wide solvent wetting and dewetting regions.[28] These arrays are among the densest, selectively deposited arrays in the literature with a density of 150–200 CNTs μm^{-1}. However, considering the high s-CNT density, the devices made from these s-CNT arrays have a notably low current. Kumar *et al.* used diazonium chemistry to pattern HfO_2 trenches with diazonium head groups to covalently react with s-CNTs.[39] While the authors were able to selectively deposit s-CNTs down to a pitch of 50 nm, the density of s-CNTs in each trench is low (~1 CNT per 50 nm trench), thereby reducing the current drive in the FETs. In addition, covalently reacting with s-CNTs to obtain spatial control leads to sp^3 defects and deterioration of electronic properties. Sun and coworkers used DNA nanotrenches to construct s-CNT arrays with a uniform pitch of 10.4 nm and a corresponding density of just under 100 CNTs μm^{-1}.[40] The DNA template and the s-CNTs were preassembled in solution and imaged on a TEM grid. In a subsequent study[41] the authors patterned a widely spaced array of 200 nm wide PMMA cavities to selectively capture the preassembled DNA templated s-CNT arrays over a 0.35 cm^2 substrate. The authors demonstrated single s-CNT per micron-scale target deposition area using sub-50 nm wide DNA templates. This approach is advantageous as the DNA trench periodicity can be varied by supramolecular assembly as the s-CNTs are preassembled in solution. However, the area of aligned s-CNTs arrays is dependent on the size of the DNA template, and the alignment of the s-CNTs is dependent on the aspect ratio of the cavities. Hence, simultaneously achieving high density of perfectly aligned s-CNTs in selective regions of the substrate on a wafer-scale without compromising on electronic properties is still an outstanding challenge.

Recently through a systematic study, we reported that varying the substrate chemistry by using self-assembled monolayers (SAMs) impacts the number density of deposited s-CNTs from solution.[42] While substrate water contact angle alone was insufficient to explain the observed s-CNT adsorption trends on these chemically modified substrates, molecular dynamics (MD) simulations provided useful mechanistic insights. In particular, the solvent-mediated affinity of polymer-wrapped s-CNTs played a key role in s-CNT deposition onto a surface. Specifically, the global minimum of the s-CNT adsorption free energy occurred in a configuration where the minimum of the solvent density around the s-CNT coincides with the minimum of the solvent density near the SAM-grafted surface. Hence, the oscillatory solvent structure near a SAM-grafted surface determines the adsorption free-energy landscape driving s-CNT deposition trends.

Building on these studies in this work, we develop chemical and topographical patterns to guide selective shear deposition of aligned array of s-CNTs from organic solvents. High shear rate deposition on chemically and topographically contrasted patterns lead to the selective-area deposition of arrays of quasi-aligned s-CNTs (~14°) even in patterns that are wider than the length of the individual nanotubes (>500 nm). However, as the width of the patterns is reduced below the length of the individual nanotubes, confinement effects dominate in the deposition process, leading to selective-area deposition of more tightly aligned s-CNTs (7°). We characterize these arrays for s-CNT density *via* scanning electron microscopy (SEM) image analysis and s-CNT alignment degree *via* a two-dimensional fast Fourier transform (2D FFT) methodology. We also demonstrate that these surface patterns can be removed after s-CNT deposition resulting in aligned, spatially selective s-CNT arrays for devices.

2. Experimental

2.1 Poly[(9,9-dioctylfluorenyl-2,7-diyl)-*alt*-*co*-(6,6′-{2,2′-bipyridine})] wrapped s-CNT solution preparation (s-CNT ink)

Chloroform s-CNT inks are prepared from isolating s-CNTs from CNT soot using a previously established procedure.[43] Briefly, a 1 : 1 ratio by weight of arc-discharge CNT soot (698695, Sigma-Aldrich) and poly[(9,9-dioctylfluorenyl-2,7-diyl)-*alt*-*co*-(6,6′-{2,2′-bipyridine})] (PFO-BPy) (American Dye Source, Inc., Quebec, Canada; #ADS153-UV) are each dispersed at a concentration of 2 mg mL^{-1} in ACS grade toluene. This solution is sonicated with a horn tip sonicator (Fisher Scientific, Waltham, MA; Sonic Dismembrator 500) and then centrifuged in a swing bucket rotor to remove undispersed material. After centrifugation, the supernatant containing polymer-wrapped s-CNTs is collected and centrifuged for an additional 18–24 h to sediment and pellet the s-CNTs. The collected s-CNT pellet is redispersed in toluene with horn tip sonication and again centrifuged. The centrifugation and sonicating process is repeated a total of three times. The final solution is prepared by horn tip sonication of the s-CNT pellet in chloroform (stabilized with ethanol). s-CNTs prepared *via* this approach are characterized by a log-normal length distribution with an average length of 580 nm and diameters varying from 1.3 to 1.8 nm.[44] Concentration of s-CNT ink was determined using optical cross sections from the

© 2021 The Author(s). Published by the Royal Society of Chemistry

Open Access Article. Published on 17 February 2021. Downloaded on 5/5/2026 7:21:35 PM.
This article is licensed under a Creative Commons Attribution-NonCommercial 3.0 Unported Licence.

CNT S_{22} transition. This solution is referred to as s-CNT ink in the manuscript.

2.2 Surface pattern fabrication on silicon oxide substrates

Surface patterns were fabricated using traditional electron-beam lithography techniques. Silicon [100] wafer substrates (Addison Engineering, Inc.) with 90 nm wet thermal silicon oxide were immersed in a 3 : 1 by volume H_2SO_4 : H_2O_2 piranha solution for 1 h at 85 °C. After piranha treatment, substrates were rinsed with deionized (DI) water and dried with N_2. For chemical patterns, ma-N 2401 resist (Micro Resist Technology) was spin coated onto the wafers and patterned using electron-beam lithography techniques. A RIE oxygen plasma for resist descum exposed the silicon oxide. The patterned substrates were submerged in octadecyltrichlorosilane (OTS) (Sigma-Aldrich, 104817) at a concentration of 5 mM in toluene for 12 h. Substrates were bath sonicated in toluene for 30 min, rinsed in toluene, and dried with N_2. Resist was stripped by submerging the substrates in anhydrous *N*-methyl-2-pyrrolidinone (NMP) (Sigma-Aldrich, 328634) for 24 h and drying with N_2. For topographical patterns, PMMA resist (MicroChem Corp.) was spin coated onto the piranha cleaned silicon substrates and an electron-beam lithography system (Elionix ELS-G100) exposed the PMMA resist with the desired pattern. After PMMA development and oxygen plasma descum, metals were evaporated onto the exposed silicon oxide. PMMA lift-off in acetone resulted in metal features on the silicon substrates.

Additional Au chemical functionalization was performed using thiol-based chemistry developed from a previous procedure.[45] Substrates with Au features were submerged in 1-octadecanethiol (OTh) (Sigma-Aldrich, O1858) at a concentration of 1 mM in ethanol for 24 h, rinsed with additional ethanol, and dried with N_2. For both OTS and OTh samples, a control water contact angle measure determined the effectiveness of SAM grafting to substrates. A 7 μL DI water droplet was dispensed using a Dataphysics OCA 15 optical contact angle measuring system on the SAM surface. Once the water droplet was fully formed, the static water contact angle (WCA) of the droplet was immediately measured. Samples were considered fully functionalized if the WCA was greater than 110°. Functionalized silicon oxide substrates were stored under N_2 until s-CNT deposition.

2.3 s-CNT array fabrication and characterization

Details of the shear system, and the shear rate control used to deposit s-CNTs, are described elsewhere.[27] Chloroform s-CNT ink was sheared across surface patterned silicon substrates at a set shear rate. Additional chloroform solvent was immediately sheared across the same substrate to remove residual s-CNTs. Substrates were boiled in toluene at 110 °C for 1 h and dried with N_2 to remove excess polymer wrapper. Substrates were stored under N_2 until characterization. Scanning electron microscope (SEM) images were taken with a Zeiss LEO 1550VP SEM. These SEM images were processed using a two-dimensional fast Fourier transform (2D FFT) algorithm to

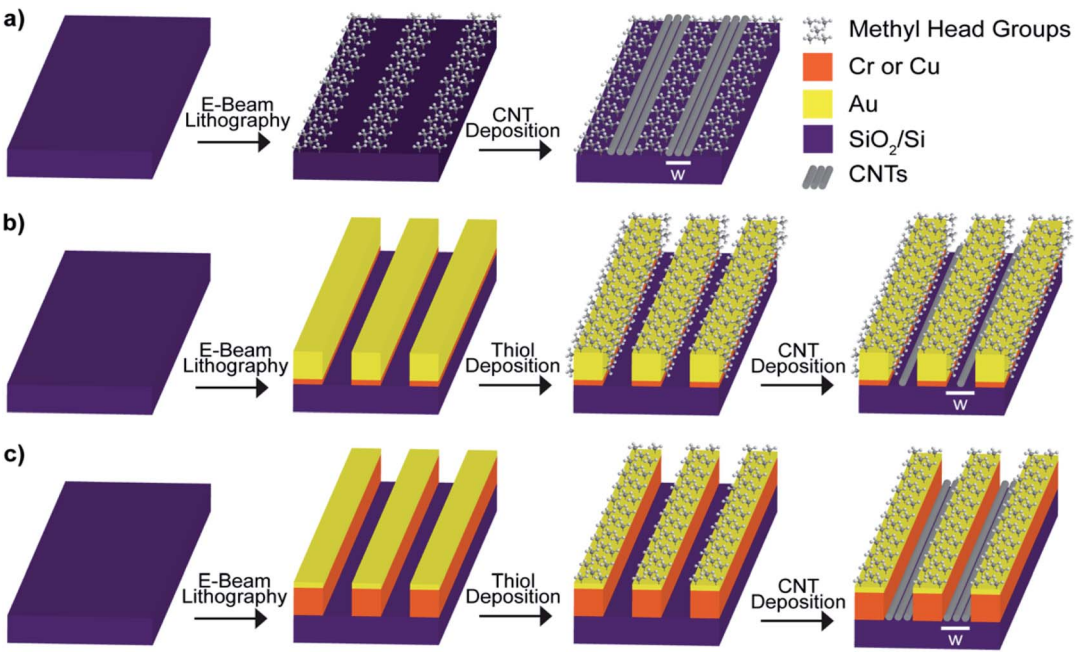

Fig. 1 Schematics for s-CNT array fabrication using (a) chemical patterns where the methyl groups represent an OTS-grafted SAM, (b) topographical patterns with SAM functionalization on both the mesa and the trench sidewall where the methyl groups represent an OTh-grafted SAM, and (c) topographical patterns with functionalization of the mesas with an OTh-grafted SAM. White line labelled '*w*' represents (a) SiO_2 stripe width and (b and c) trench width.

© 2021 The Author(s). Published by the Royal Society of Chemistry

Open Access Article. Published on 17 February 2021. Downloaded on 5/5/2026 7:21:35 PM.
This article is licensed under a Creative Commons Attribution-NonCommercial 3.0 Unported Licence.

determine s-CNT alignment. The 2D FFT methodology is described in detail in ESI Fig. S2–S5.†

2.4 Topographical pattern removal

Topographical pattern trenches were removed by etching away the metal between the s-CNT arrays. A thin layer of PMMA was spin coated onto the s-CNTs prior to metal removal to protect the s-CNTs from the metal etchant. Any s-CNTs crossing over the gold mesas were first removed using an oxygen plasma reactive-ion etching procedure (see ESI Fig. S16†). Metal trenches (Au/Cu) were removed by submerging substrates in a standard gold etchant (Sigma-Aldrich, 651818) for 5 min and soaking the samples in DI water for 10 min. The iodine-based gold etchant converted Cu to a copper iodine complex that is insoluble in aqueous solution. This process was repeated once to completely convert all Cu. PMMA protective layer and copper iodine complex was removed by boiling acetone at 110 °C for 15 minutes.

Raman spectroscopy measurements of s-CNTs were taken on a Thermo Scientific DXRxi Raman imaging microscope using the mapping function. Raman maps of the s-CNT characteristic bands over 34 × 34 μm^2 areas were taken consisting of 1156 pixels where a pixel represents a 1 μm^2 area.

3. Results and discussion

3.1 Chemical patterns for s-CNT arrays

We first explored the effectiveness of chemical pattern contrast for selective deposition of s-CNT arrays by shear from an organic ink. The polymer-wrapped s-CNTs prefer to adsorb on SiO_2 compared to octadecylsilane (OTS)-grafted silicon oxide due to solvent structure effects.[42] To take advantage of s-CNT adsorption preferences to drive selective-area deposition, alternating stripes of SiO_2 and OTS were patterned using an electron-beam lithography (EBL) process illustrated in Fig. 1a. Initial studies using PMMA resist for patterning resulted in the penetration of the OTS through the resist to the substrate during the liquid deposition, hence a negative tone resist was selected to mitigate this problem. The crosslinking in the negative tone resist prevented penetration of OTS into the resist during selective functionalization (ESI Fig. S1†). After OTS functionalization, the negative tone resist was removed resulting in a chemically patterned silicon substrate consisting of alternating stripes of SiO_2 and OTS depicted in Fig. 1a. Individual stripes widths were varied between 250 and 2000 nm where the width of the SiO_2 stripes in the chemical pattern is defined as w (illustrated in Fig. 1a). The OTS stripe width in a chemical pattern is also equal to w at a given SiO_2 stripe width.

On these chemically patterned substrates, 375 μL of s-CNT ink at a concentration of 240 μg mL^{-1} was deposited using a previously established shear deposition method[27] at a high shear rate of 46 000 s^{-1}. These experimental deposition conditions were based on our prior work on optimizing CNT alignment by shear deposition, which resulted in the best alignment.[27] Fig. 2a shows the SEM images of s-CNTs deposited on alternating SiO_2 and OTS stripes fabricated using EBL. From these SEM images, as expected the s-CNT density was significantly higher on SiO_2, the favorable s-CNT adsorption surface, compared to OTS, the unfavorable adsorption surface.

Fig. 2 shows s-CNT deposition on the chemically patterned substrates. Alignment of s-CNTs in these arrays was characterized by two-dimensional fast Fourier transform (2D FFT)

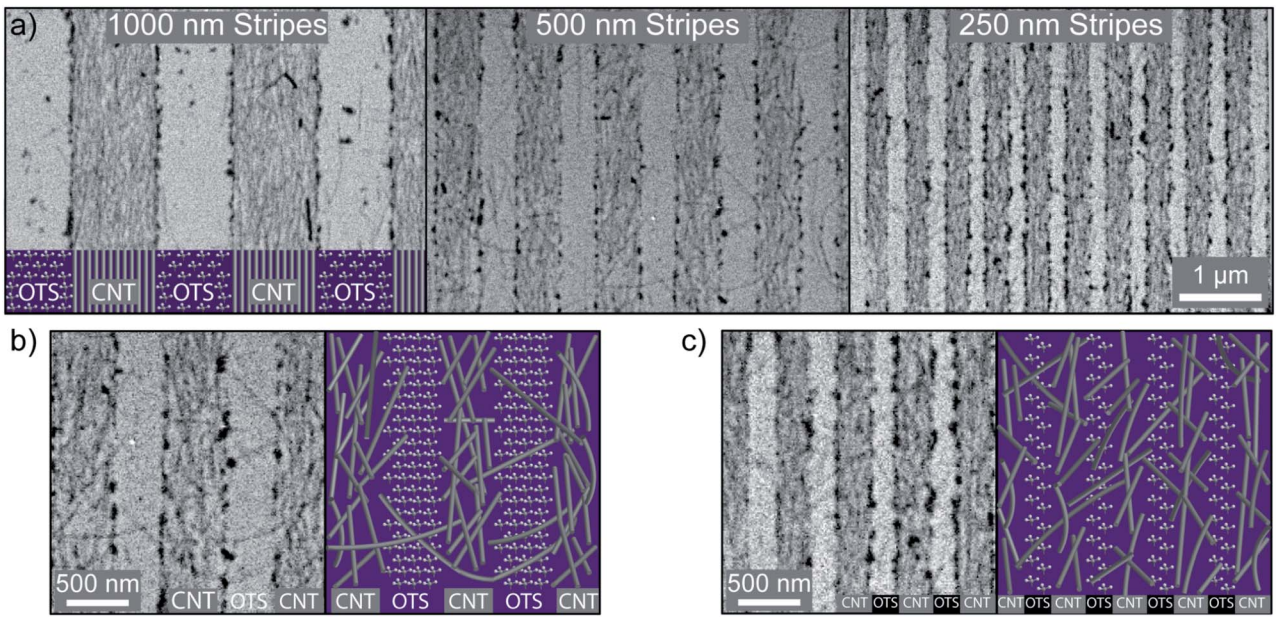

Fig. 2 (a) SEM images of PFO-BPy wrapped s-CNTs shear deposited across alternating OTS (bright) and SiO_2 (dark) stripes. From left to right, SiO_2 stripes are 1000, 500, and 250 nm wide. Scale bar is 1 micron for all images. (b and c) High resolution SEM images of (b) 500 nm and (c) 250 nm wide SiO_2 stripes show the s-CNTs pinned from SiO_2 stripes across the OTS stripes. Cartoon (right) depict the location of these pinned s-CNTs.

© 2021 The Author(s). Published by the Royal Society of Chemistry

Open Access Article. Published on 17 February 2021. Downloaded on 5/5/2026 7:21:35 PM.
This article is licensed under a Creative Commons Attribution-NonCommercial 3.0 Unported Licence.

analysis of SEM images for the deposited s-CNT arrays. In the literature 2D FFT analysis has been used for characterizing alignment of various types of fibrous materials[46,47] including CNT arrays.[48] Details of the 2D FFT methodology are in ESI Fig. S2–S5.† The orientation distribution derived from the 2D FFT methodology was fitted with a Gaussian distribution, and the s-CNT alignment degree was quantified by calculating the standard deviation (σ) of this curve. As the SiO_2 stripe width w decreases from 2000 nm down to 250 nm, s-CNT alignment stayed constant at a σ of around 18° (ESI Fig. S6†). Visual inspection of the images shows a number of s-CNTs that are pinned at the edges of SiO_2 stirpes and extend onto the OTS region as shown in Fig. 2b and c. Part of these s-CNTs are favorably adsorbed to the SiO_2 region but part are unfavorably adsorbed to the OTS. The chemical contrast alone is not strong enough to prevent the deposition of these s-CNTs, which are often poorly aligned. Increasing the spacing between the SiO_2 stripes to 5000 nm did not significantly reduce CNT pinning at the edges of the pattern or improve the resulting σ, evidencing that the deposition of these s-CNTs is not driven by bridging from one SiO_2 region to the next (ESI Fig. S7†). Additionally, increasing the spacing between SiO_2 stripes is not practical when fabricating dense sets of devices on a single substrate, which required us to focus further efforts on reducing this pinning of s-CNTs across stripes.

3.2 Topographical patterns for s-CNT arrays

We hypothesized that addition of a physical barrier to the chemical patterns on the silicon substrate would both significantly improve s-CNT alignment on SiO_2 stripes as well as limit pinning across OTS stripes. The design and fabrication of the topographical surface patterns with integrated chemical patterns are illustrated in Fig. 1b and c. The trench floors were bare SiO_2 acting as the favorable s-CNT deposition surface while the mesas acted as the unfavorable deposition surface. The mesas needed to be fabricated from a material that could be selectively functionalized without modifying SiO_2 on the trench floor. For fabrication simplicity, we picked gold for the mesas as it could be selectively functionalized with octadecanethiol (OTh), a thiol terminated OTS. To improve adhesion of gold to SiO_2 substrate, chromium or copper was used as an adhesion layer. The height of the Au/Cr stack was 25 nm, a value 10–20 times greater than the diameter of the s-CNTs.[44] Functionalization of Au with OTh prevented s-CNTs from depositing onto the Au surface (ESI Fig. S8†). Trenches, consisting of 22.5 nm Au on 2.5 nm Cr, led to functionalization of Au with OTh on both the mesas and the side walls (Fig. 1b). However, the overall density of the s-CNTs deposited in these patterns was an order of magnitude lower than on bulk SiO_2 substrates, possibly due to the disruption of solvent structure along the Au sidewalls (ESI Fig. S9†). To reduce the thickness of Au, the procedure outlined in Fig. 1c, with a thin 2.5 nm Au top layer and 22.5 nm Cr in the 25 nm Au/Cr metal stripe stack, was implemented to prevent OTh functionalization of the trench sidewalls.

These modified patterns were effective in increasing the density of the deposited s-CNTs from approximately 5–10 to over 30 CNTs μm^{-1} in the trenches while minimizing their deposition on the mesas (Fig. 3a). By averaging the number of s-CNTs in five trenches, their density as a function of both w and deposition shear rate was quantified (ESI Fig. S10†). At a constant deposition shear rate of 4600 s^{-1}, the s-CNT density was relatively constant at 32–36 CNTs μm^{-1} even when w was varied from 100–1000 nm. Inherently larger error bars were observed for narrower trenches due to the lower number of s-CNTs. For the shear rates ranging from 46 to 46 000 s^{-1}, the s-CNT density again remained constant around 32–35 CNTs μm^{-1}, when w was fixed at 250 nm. The lack of any dependence of s-CNT density on either shear rate or trench width strongly suggests that the mechanism of the s-CNT deposition process dominates over processing parameters. While s-CNT density can potentially be increased by increasing s-CNT ink concentration, larger changes would likely require a change in the s-CNT deposition method.[49]

The 2D FFT metrology method was applied to quantify the s-CNT alignment in these topographical patterns as discussed earlier. Fig. 3b shows σ from the aligned s-CNT arrays as a function of both shear rate and trench width. The bulk data points are defined as s-CNT deposition on unpatterned, planar SiO_2. For the 2D FFT analysis a standard deviation greater than 30°, corresponding to non-preferentially oriented s-CNT films, was defined as the maximum limit. Visual inspection of SEM images of both a low shear rate (46 s^{-1}) in the 2000 nm wide trenches as well as bulk samples confirmed the random distribution (ESI Fig. S11†) with a $\sigma > 30°$. As expected, at a constant w, s-CNT alignment improved with increasing shear rate. At a constant shear rate, s-CNT alignment also improved with decreasing w down to 100 nm. The best alignment with a σ of $7.6 \pm 0.3°$ was observed at a shear rate of 4600 s^{-1} in 100 nm trenches. Fig. 3c shows SEM images of s-CNT arrays in multiple trenches stitched together (denoted by red marks) highlighting the dramatically improved s-CNT alignment in narrower trenches compared to bulk deposition for a given shear rate.

The studies presented here uncover important guidelines to achieving exceptionally aligned s-CNT arrays while selectively depositing them in desired regions of the substrate. These studies confirm that, as on planar substrates,[27] increasing the shear rate during s-CNT deposition does not indefinitely increase their alignment in the trenches. When the patterns are wider than the length of the s-CNT (>500 nm), increase in shear rate leads to quasi aligned CNTs, with a σ of ~14°. For example, while increasing shear rate from 46 s^{-1} to 4600 s^{-1} dramatically improved the alignment from $28.5 \pm 6.3°$ to $16.2 \pm 1.3°$ in 1000 nm wide trenches, a further increase to 46 000 s^{-1} resulted in a marginal improvement to a σ of $13.3 \pm 1.0°$. When the pattern width is reduced to less than the length of the individual s-CNTs (<500 nm), confinement effects dominate over shear rate, leading to a dramatic enhancement in the alignment degree. For example, using a low shear rate of 46 s^{-1} with a 100 nm wide trench achieved an alignment degree of $7.6 \pm 1.3°$. This alignment degree is remarkable in comparison to the alignment degree of $19.3 \pm 3.5°$ at the high shear rate (46 000 s^{-1}) on planar SiO_2 (ESI Fig. S12†).

© 2021 The Author(s). Published by the Royal Society of Chemistry

Open Access Article. Published on 17 February 2021. Downloaded on 5/5/2026 7:21:35 PM.
This article is licensed under a Creative Commons Attribution-NonCommercial 3.0 Unported Licence.

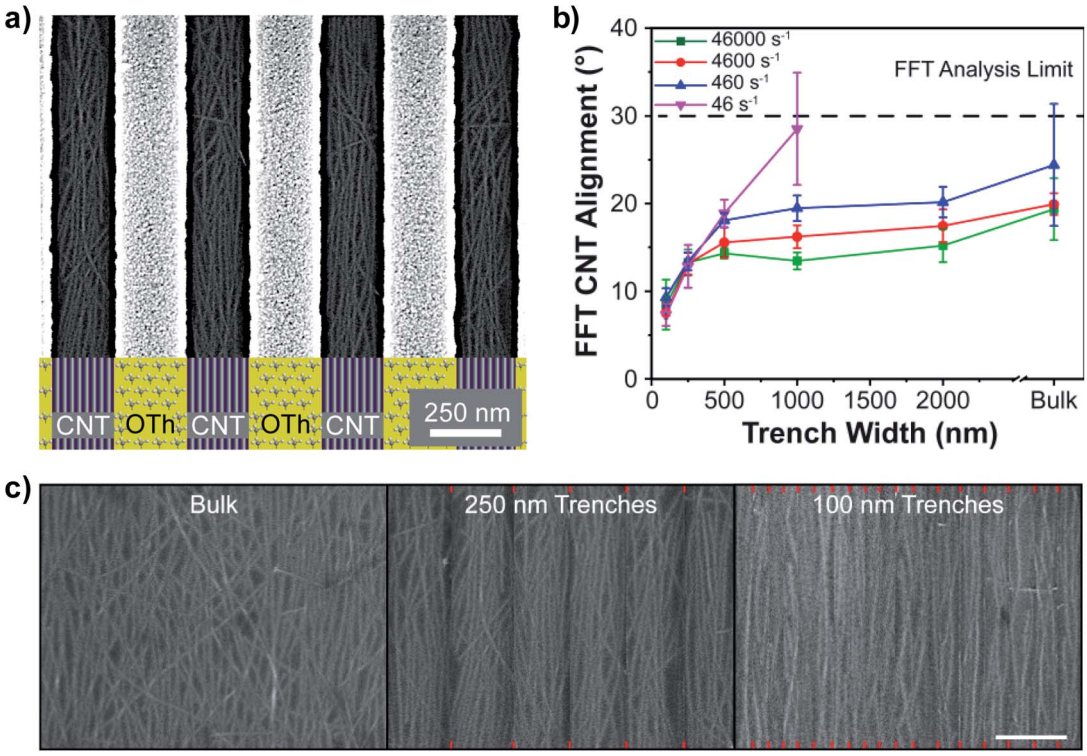

Fig. 3 (a) SEM image of s-CNT arrays in 250 nm wide trenches where s-CNTs were deposited at a shear rate of 4600 s^{-1} in 25 nm tall OTh-grafted Au/Cr trenches. (b) Plot of CNT alignment degree as characterized by the standard deviation (σ) from the 2D FFT analysis as a function of both trench width and shear rate. (c) Side-by side comparison of representative SEM images at constant deposition shear rate of 4600 s^{-1} for bulk, 250 nm, and 100 nm wide trenches demonstrating s-CNT alignment improvement as trench width decreases. Images for 250 and 100 nm wide trenches contain multiple individual trenches adjacent to each other stitched together (red ticks show stitch locations). Scale bar is 250 nm and same for all images.

Chemical patterns alone consisting of alternating OTS and SiO_2 stripes resulted in a constant s-CNT alignment degree ~18° regardless of the stripe width. Whereas the addition of a topographical pattern consisting of 25 nm tall metal stripes improved s-CNT alignment from 19.3 ± 3.5° at a deposition shear rate of 46 000 s^{-1} on bulk SiO_2 to 8.5 ± 2.8° in 100 nm wide trenches. Hence, the alignment can be improved by decreasing the trench width provided both the trench width is sufficiently narrow (<500 nm) and the trench height is sufficiently high to prevent s-CNTs from depositing on multiple SiO_2 stripes. Based on experimental results, trench heights over 25 nm did not further improve s-CNT alignment degree (ESI Fig. S13†). s-CNT alignment on these patterned substrates is uniform across the 2 × 3 cm^2 SiO_2/Si substrates (ESI Fig. S14†) demonstrating the inherent scalability of this process. Larger area deposition can be achievable in future by scaling up of the shear deposition system as shown in our prior work on unpatterned substrates.[27]

Another important criterion for this pattern design to be compatible with device fabrication is to completely remove any residual metals post-CNT deposition. For these experiments, Cr, a traditional adhesion layer for Au, was substituted with Cu in the fabrication scheme shown in Fig. 1c because standard Cr etchants attack a PMMA protective layer on the CNTs unlike Cu etchants.[50] SEM images of s-CNT arrays before (Fig. 4a) and after (Fig. 4b) trench removal confirm that the alignment of the s-CNT was preserved (ESI Fig. S15 and S16†), making this removal process compatible with FET device fabrication. Another consequence of the trench removal process is that any crossing nanotubes that might bridge between the SiO_2 stripes, are also removed.

To ensure the electronic properties of the s-CNTs are preserved, we examined the Raman spectrum of s-CNTs before and after exposure to Au/Cu trench removal treatments. Analysis of the ratio of D to G band intensities (I_D/I_G) is commonly used in the literature to examine electronic defects in CNTs.[51] We use spin coated s-CNTs on 90 nm SiO_2/Si substrates for these tests to increase the signal of G, D, 2D, and Si Raman peaks. These samples were subjected to the same trench removal process as used in Fig. 4. Raman spectra of s-CNTs were taken over a 34 μm^2 area and average into a single spectra (ESI Fig. S17†). Fig. 4d shows the averaged Raman spectra of the s-CNTs before and after trench removal. Before processing, the I_D/I_G of the s-CNTs is 0.20 ± 0.02. After the trench removal process, s-CNTs have an I_D/I_G of 0.15 ± 0.02. These data show the trench removal process does not adversely affect the electronic properties of the CNTs. The slight improvement in the I_D/I_G is likely due to increased removal of residual polymer-wrapper[52] due to the gold etchant. Adsorbates on CNTs will also suppress G band intensity,[53] hence lowering I_D/I_G. These results confirm that the electronic quality of the starting s-CNTs is preserved

© 2021 The Author(s). Published by the Royal Society of Chemistry

Open Access Article. Published on 17 February 2021. Downloaded on 5/5/2026 7:21:35 PM.
This article is licensed under a Creative Commons Attribution-NonCommercial 3.0 Unported Licence.

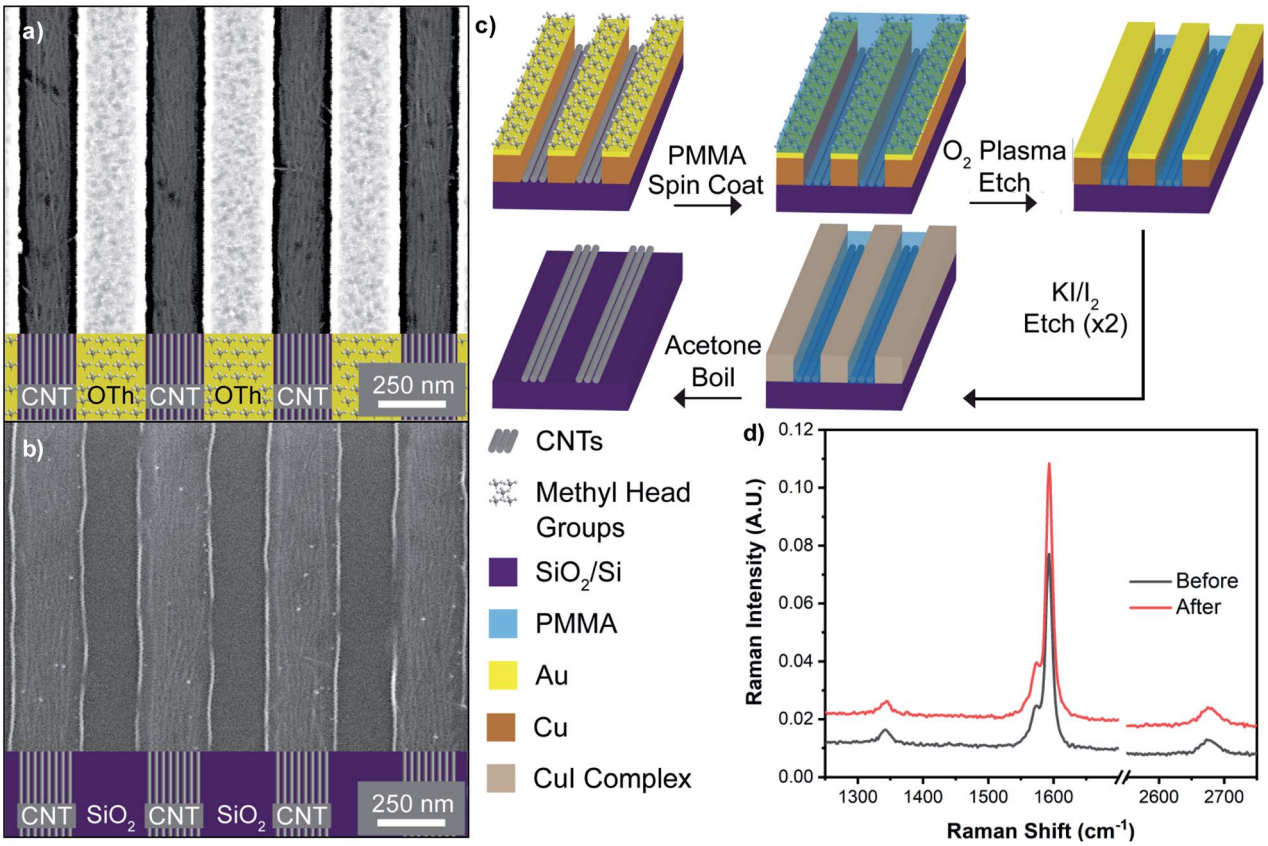

Fig. 4 SEM images of PFO-BPy wrapped s-CNTs sheared at 4600 s^{-1} across 250 nm OTh–SiO_2 wide trench arrays (a) before and (b) after Cu/Au trench removal. (c) Process schematic for trench removal. (d) Plot showing averaged Raman spectra over a 34 μm^2 area of CNTs before and after trench removal normalized to the Si peak. "After" spectrum is offset by 0.01 to improve readability.

throughout the processing steps, making this removal process compatible with FET device fabrication.

4. Conclusion

In conclusion, we have exploited chemical and topographical patterns in concert with shear forces to selectively deposit a tightly aligned array of s-CNTs. Chemical contrast on a SiO_2/Si substrate was created by alternate stripes of SiO_2 and OTS-grafted SiO_2. During shear deposition, s-CNTs deposited preferentially on the SiO_2 stripes compared to OTS stripes. However, the alignment degree of s-CNT arrays was similar to unpatterned substrates and could not prevent pinning of CNTs between adjacent SiO_2 stripes. This problem was addressed by introduction of topography with the chemical pattern to deposit s-CNTs by shear. The role of shear and confinement by the topographical features was delineated through a series of studies. Pre-alignment of s-CNTs *via* shear plays a major role when the trench width is greater than 500 nm or larger than the length of the s-CNTs. However, when the trench width decreases below 500 nm, the confinement effect dominates over shear. At a trench width of 100 nm, exceptional degree of alignment (with a σ of 7.6 $\pm$ 0.3° at a shear rate of 4600 s^{-1}), was achieved while maintaining a density greater than 30 CNTs μm^{-1}. The rotational diffusion coefficient is expected to quickly decrease, as the s-CNT length increases, thereby aiding in shear alignment.[44,54] Hence, the pre-alignment by shear forces and confinement effect in trenches can both be potentially enhanced by increasing the average s-CNT length. Additionally, these topographical patterns can be removed post-CNT deposition using standard solution processing steps to obtain aligned s-CNT arrays on SiO_2 for device fabrication without altering the alignment. While chemical contrast alone enables selective-area deposition, chemical contrast in addition to topography enables more effective selective-area deposition, stronger confinement effects, and the removal of nanotubes deposited in spurious areas *via* selective lift-off of the topographical features. Since this methodology relies on traditional fabrication and substrate modification methods, it is inherently scalable and provides a means to fabricate spatially selective, aligned s-CNT arrays for next-generation semiconducting devices.

Conflicts of interest

There are no conflicts to declare.

Acknowledgements

J. H. D., A. S., K. R. J., M. S. A., A. B., P. G. acknowledge funding from NSF SNM-IS award no 1727523. J. H. D. acknowledges

Open Access Article. Published on 17 February 2021. Downloaded on 5/5/2026 7:21:35 PM.
This article is licensed under a Creative Commons Attribution-NonCommercial 3.0 Unported Licence.

partial support from the PPG Industries sponsored fellowship. Raman spectroscopy and mapping conducted by X. Z. and M. S. A. supported by U.S. Department of Energy, Office of Science, Basic Energy Sciences, under award no. DE-SC0016007. We acknowledge S. Foradori for insightful discussions on removal of the topographical patterns. The authors gratefully acknowledge use of facilities and instrumentation at the University of Wisconsin–Madison Wisconsin Centers for Nanoscale Technology partially supported by the NSF through the University of Wisconsin Materials Research Science and Engineering Center (DMR-1720415). Portions of this work were done using an electron-beam lithography tool at the University of Wisconsin Nanoscale Fabrication Center. We acknowledge support from the NSF (DMR-1625348) for the acquisition of this tool.

References

1 P. Avouris, Z. Chen and V. Perebeinos, *Nat. Nanotechnol.*, 2007, **2**, 605–615.
2 T. Dürkop, S. A. Getty, E. Cobas and M. S. Fuhrer, *Nano Lett.*, 2004, **4**, 35–39.
3 Y. I. Jhon, C. Kim, M. Seo, W. J. Cho, S. Lee and Y. M. Jhon, *Sci. Rep.*, 2016, **6**, 20324.
4 S.-Y. Yue, T. Ouyang and M. Hu, *Sci. Rep.*, 2015, **5**, 15440.
5 G. S. Tulevski, A. D. Franklin, D. Frank, J. M. Lobez, Q. Cao, H. Park, A. Afzali, S.-J. Han, J. B. Hannon and W. Haensch, *ACS Nano*, 2014, **8**, 8730–8745.
6 J. Zhang, A. Lin, N. Patil, H. Wei, L. Wei, H. P. Wong and S. Mitra, *IEEE Trans. Comput. Aided Des. Integrated Circ. Syst.*, 2012, **31**, 453–471.
7 S. J. Kang, C. Kocabas, T. Ozel, M. Shim, N. Pimparkar, M. A. Alam, S. V. Rotkin and J. A. Rogers, *Nat. Nanotechnol.*, 2007, **2**, 230–236.
8 D. Janas, *Mater. Chem. Front.*, 2018, **2**, 36–63.
9 A. Nish, J.-Y. Hwang, J. Doig and R. J. Nicholas, *Nat. Nanotechnol.*, 2007, **2**, 640–646.
10 F. Léonard, *Nanotechnology*, 2006, **17**, 2381–2385.
11 L. Kang, S. Zhang, Q. Li and J. Zhang, *J. Am. Chem. Soc.*, 2016, **138**, 6727–6730.
12 J. Si, D. Zhong, H. Xu, M. Xiao, C. Yu, Z. Zhang and L.-M. Peng, *ACS Nano*, 2018, **12**, 627–634.
13 W. Liu, S. Zhang, L. Qian, D. Lin and J. Zhang, *Carbon*, 2020, **157**, 164–168.
14 Y. Hu, L. Kang, Q. Zhao, H. Zhong, S. Zhang, L. Yang, Z. Wang, J. Lin, Q. Li, Z. Zhang, L. Peng, Z. Liu and J. Zhang, *Nat. Commun.*, 2015, **6**, 6099.
15 S. H. Jin, S. N. Dunham, J. Song, X. Xie, J.-h. Kim, C. Lu, A. Islam, F. Du, J. Kim, J. Felts, Y. Li, F. Xiong, M. A. Wahab, M. Menon, E. Cho, K. L. Grosse, D. J. Lee, H. U. Chung, E. Pop, M. A. Alam, W. P. King, Y. Huang and J. A. Rogers, *Nat. Nanotechnol.*, 2013, **8**, 347–355.
16 G. S. Tulevski, A. D. Franklin and A. Afzali, *ACS Nano*, 2013, **7**, 2971–2976.
17 S. Zhang, L. Kang, X. Wang, L. Tong, L. Yang, Z. Wang, K. Qi, S. Deng, Q. Li, X. Bai, F. Ding and J. Zhang, *Nature*, 2017, **543**, 234–238.
18 M. He, X. Wang, S. Zhang, H. Jiang, F. Cavalca, H. Cui, J. B. Wagner, T. W. Hansen, E. Kauppinen, J. Zhang and F. Ding, *Sci. Adv.*, 2019, **5**, eaav9668.
19 T. Fujigaya and N. Nakashima, *Sci. Technol. Adv. Mater.*, 2015, **16**, 024802.
20 Q. Cao, S.-j. Han, G. S. Tulevski, Y. Zhu, D. D. Lu and W. Haensch, *Nat. Nanotechnol.*, 2013, **8**, 180.
21 X. Li, L. Zhang, X. Wang, I. Shimoyama, X. Sun, W.-S. Seo and H. Dai, *J. Am. Chem. Soc.*, 2007, **129**, 4890–4891.
22 V. Sgobba, G. Giancane, D. Cannoletta, A. Operamolla, O. Hassan Omar, G. M. Farinola, D. M. Guldi and L. Valli, *ACS Appl. Mater. Interfaces*, 2014, **6**, 153–158.
23 X. He, W. Gao, L. Xie, B. Li, Q. Zhang, S. Lei, J. M. Robinson, E. H. Hároz, S. K. Doorn, W. Wang, R. Vajtai, P. M. Ajayan, W. W. Adams, R. H. Hauge and J. Kono, *Nat. Nanotechnol.*, 2016, **11**, 633.
24 S. Kaida, J. Matsui, T. Sagae, Y. Hoshikawa, T. Kyotani and T. Miyashita, *Carbon*, 2013, **59**, 503–511.
25 C. Zamora-Ledezma, C. Blanc, M. Maugey, C. Zakri, P. Poulin and E. Anglaret, *Nano Lett.*, 2008, **8**, 4103–4107.
26 E. M. Remillard, Z. Branson, J. Rahill, Q. Zhang, T. Dasgupta and C. D. Vecitis, *Nanoscale*, 2017, **9**, 6854–6865.
27 K. R. Jinkins, J. Chan, R. M. Jacobberger, A. Berson and M. S. Arnold, *Adv. Electron. Mater.*, 2019, **5**, 1800593.
28 S. Park, G. Pitner, G. Giri, J. H. Koo, J. Park, K. Kim, H. Wang, R. Sinclair, H. S. P. Wong and Z. Bao, *Adv. Mater.*, 2015, **27**, 2656–2662.
29 M. Engel, J. P. Small, M. Steiner, M. Freitag, A. A. Green, M. C. Hersam and P. Avouris, *ACS Nano*, 2008, **2**, 2445–2452.
30 G. L. Goh, N. Saengchairat, S. Agarwala, W. Y. Yeong and T. Tran, *Nanoscale*, 2019, **11**, 10603–10614.
31 G. L. Goh, S. Agarwala and W. Y. Yeong, *ACS Appl. Mater. Interfaces*, 2019, **11**, 43719–43730.
32 C. Lan, M. Guo, C. Li, Y. Qiu, Y. Ma and J. Sun, *ACS Appl. Mater. Interfaces*, 2020, **12**, 7477–7485.
33 G. L. Goh, S. Agarwala and W. Y. Yeong, *Adv. Mater. Interfaces*, 2019, **6**, 1801318.
34 B. Herren, T. Gu, Q. Tang, M. Saha and Y. Liu, *ASME International Mechanical Engineering Congress and Exposition*, 2019, V012T10A019.
35 J. M. D'Arcy, H. D. Tran, A. Z. Stieg, J. K. Gimzewski and R. B. Kaner, *Nanoscale*, 2012, **4**, 3075–3082.
36 Y. Joo, G. J. Brady, M. S. Arnold and P. Gopalan, *Langmuir*, 2014, **30**, 3460–3466.
37 L. Liu, J. Han, L. Xu, J. Zhou, C. Zhao, S. Ding, H. Shi, M. Xiao, L. Ding, Z. Ma, C. Jin, Z. Zhang and L.-M. Peng, *Science*, 2020, **368**, 850.
38 C. Klinke, J. B. Hannon, A. Afzali and P. Avouris, *Nano Lett.*, 2006, **6**, 906–910.
39 B. Kumar, A. L. Falk, A. Afzali, G. S. Tulevski, S. Oida, S.-J. Han and J. B. Hannon, *ACS Nano*, 2017, **11**, 7697–7701.
40 W. Sun, J. Shen, Z. Zhao, N. Arellano, C. Rettner, J. Tang, T. Cao, Z. Zhou, T. Ta, J. K. Streit, J. A. Fagan, T. Schaus, M. Zheng, S.-J. Han, W. M. Shih, H. T. Maune and P. Yin, *Science*, 2020, **368**, 874.

© 2021 The Author(s). Published by the Royal Society of Chemistry

Open Access Article. Published on 17 February 2021. Downloaded on 5/5/2026 7:21:35 PM.
This article is licensed under a Creative Commons Attribution-NonCommercial 3.0 Unported Licence.

41 M. Zhao, Y. Chen, K. Wang, Z. Zhang, J. K. Streit, J. A. Fagan, J. Tang, M. Zheng, C. Yang, Z. Zhu and W. Sun, *Science*, 2020, **368**, 878.
42 J. H. Dwyer, Z. Shen, K. R. Jinkins, W. Wei, M. S. Arnold, R. C. Van Lehn and P. Gopalan, *Langmuir*, 2019, **35**, 12492–12500.
43 G. J. Brady, A. J. Way, N. S. Safron, H. T. Evensen, P. Gopalan and M. S. Arnold, *Sci. Adv.*, 2016, **2**, e1601240.
44 G. J. Brady, Y. Joo, M.-Y. Wu, M. J. Shea, P. Gopalan and M. S. Arnold, *ACS Nano*, 2014, **8**, 11614–11621.
45 H. Yeon, C. Wang, R. C. Van Lehn and N. L. Abbott, *Langmuir*, 2017, **33**, 4628–4637.
46 C. E. Ayres, B. S. Jha, H. Meredith, J. R. Bowman, G. L. Bowlin, S. C. Henderson and D. G. Simpson, *J. Biomater. Sci., Polym. Ed.*, 2008, **19**, 603–621.
47 E. E. Morrill, A. N. Tulepbergenov, C. J. Stender, R. Lamichhane, R. J. Brown and T. J. Lujan, *Biomech. Model. Mechanobiol.*, 2016, **15**, 1467–1478.
48 E. Brandley, E. S. Greenhalgh, M. S. P. Shaffer and Q. Li, *Carbon*, 2018, **137**, 78–87.
49 J. Zhang, J. Cui, F. Wei, W. Wang, X. He and X. Mei, *Appl. Surf. Sci.*, 2020, **504**, 144397.
50 K. R. Williams, K. Gupta and M. Wasilik, *J. Microelectromech. Syst.*, 2003, **12**, 761–778.
51 M. J. Shea, J. Wang, J. T. Flach, M. T. Zanni and M. S. Arnold, *APL Mater.*, 2018, **6**, 056104.
52 C. Kanimozhi, G. J. Brady, M. J. Shea, P. Huang, Y. Joo, M. S. Arnold and P. Gopalan, *ACS Appl. Mater. Interfaces*, 2017, **9**, 40734–40742.
53 M. R. Kagan and R. L. McCreery, *Langmuir*, 1995, **11**, 4041–4047.
54 M. M. Tirado, C. L. Martínez and J. G. de la Torre, *J. Chem. Phys.*, 1984, **81**, 2047–2052.

© 2021 The Author(s). Published by the Royal Society of Chemistry